International Journal of Nanomedicine

Dovepress
Taylor & Francis Group

Open Access Full Text Article

ORIGINAL RESEARCH

Melanin@PLGA/Nuciferine Nanoparticles for Enhanced Photothermal Therapy of Hepatocellular Carcinoma by Promoting Autophagy

Yingxuan Mao[1], Xinling Du[1,2], Weidong Wang[1], Tianxiu Dong[1], Mingwei Zhu[1], Jiamei Niu[1], Mingming Li[1], Jian Jiang[1], Linlin Han[1], Xiuhua Yang[1]

[1]Department of Ultrasound, The First Affiliated Hospital of Harbin Medical University, Harbin, 150001, People's Republic of China; [2]Department of Ultrasound, The Second Affiliated Hospital of Heilongjiang University of Chinese Medicine, Harbin, 150001, People's Republic of China

Correspondence: Xiuhua Yang, Department of Ultrasound, The First Affiliated Hospital of Harbin Medical University, Harbin, 150001, People's Republic of China, Email yangxiuhua@hrbmu.edu.cn

Background: The advent of nanotechnology has enabled photothermal therapy (PTT) to emerge as a novel, noninvasive modality for thermal ablation of hepatocellular carcinoma (HCC). However, the thermal stress induced by PTT can trigger autophagy in tumor cells, contributing to treatment resistance. Consequently, a promising strategy to enhance PTT efficacy involves concurrently disrupting tumor cell autophagy, given that autophagy overactivation can ultimately induce cell death.

Methods: MPN was designed for precise magnetic resonance imaging (MRI) diagnosis of HCC and guidance of PTT for HCC. PTT-mediated heating accelerated nuciferine release from the MPN. The released nuciferine then promoted autophagosome formation and autophagic degradation, thereby enhancing PTT efficacy via autophagy overactivation.

Results: MPN successfully encapsulated melanin and loaded nuciferine, exhibiting favorable encapsulation efficiency and drug-loading capacity. Upon 808 nm near-infrared (NIR) irradiation, MPN exhibited excellent photothermal conversion efficiency and robust stability. In vitro experiments confirmed that nuciferine effectively promoted autophagosome maturation in HCC cells, with enhanced autophagy induction observed when it was combined with PTT. Furthermore, MPN exhibited high MRI contrast. In vivo studies validated its selective accumulation in HCC tumors, enabling safe and effective thermal ablation and subsequent suppression of post ablation HCC growth via autophagy overexpression.

Conclusion: MPN enhanced the T1-weighted MRI signal for accurate tumor localization and demonstrated superior photothermal properties. Moreover, MPN potentiated PTT by inducing autophagy overactivation in HCC cells, thereby enhancing ablation efficacy and inhibiting post-PTT tumor growth.

Keywords: photothermal therapy, hepatocellular carcinoma, nanoparticles, autophagy

Introduction

Hepatocellular carcinoma (HCC) accounts for 90% of primary liver cancers and is currently recognized as the sixth most common type of cancer and the fourth leading cause of cancer-related death worldwide.[1–3] Clinical studies have demonstrated the efficacy of ultrasound-guided radiofrequency ablation in thermally ablating HCC cells.[4–6] Furthermore, noninvasive thermal ablation techniques are gaining attention as viable options for HCC treatment. Recent advancements in nanotechnology have facilitated the emergence of photothermal therapy (PTT) as an innovative, noninvasive cancer treatment characterized by its targeted ablation capabilities and straightforward operational procedures.[7–9] Nanocarriers deliver photothermal conversion agents to the tumor site, promoting their accumulation.[10,11] When subjected to near-infrared (NIR) light, these agents generate heat to increase the temperature in the targeted area and induce damage to tumor cells.

Melanin (Mel), a naturally occurring photothermal conversion agent, absorbs a wide range of light wavelengths and exhibits enhanced photothermal properties due to the large number of unsaturated bonds in its molecular structure.[12,13] Unlike other photothermal agents, Mel is metabolized by the hepatobiliary system, thereby reducing the risk of prolonged retention in

Received: 24 April 2025
Accepted: 2 September 2025
Published: 10 September 2025

Graphical Abstract

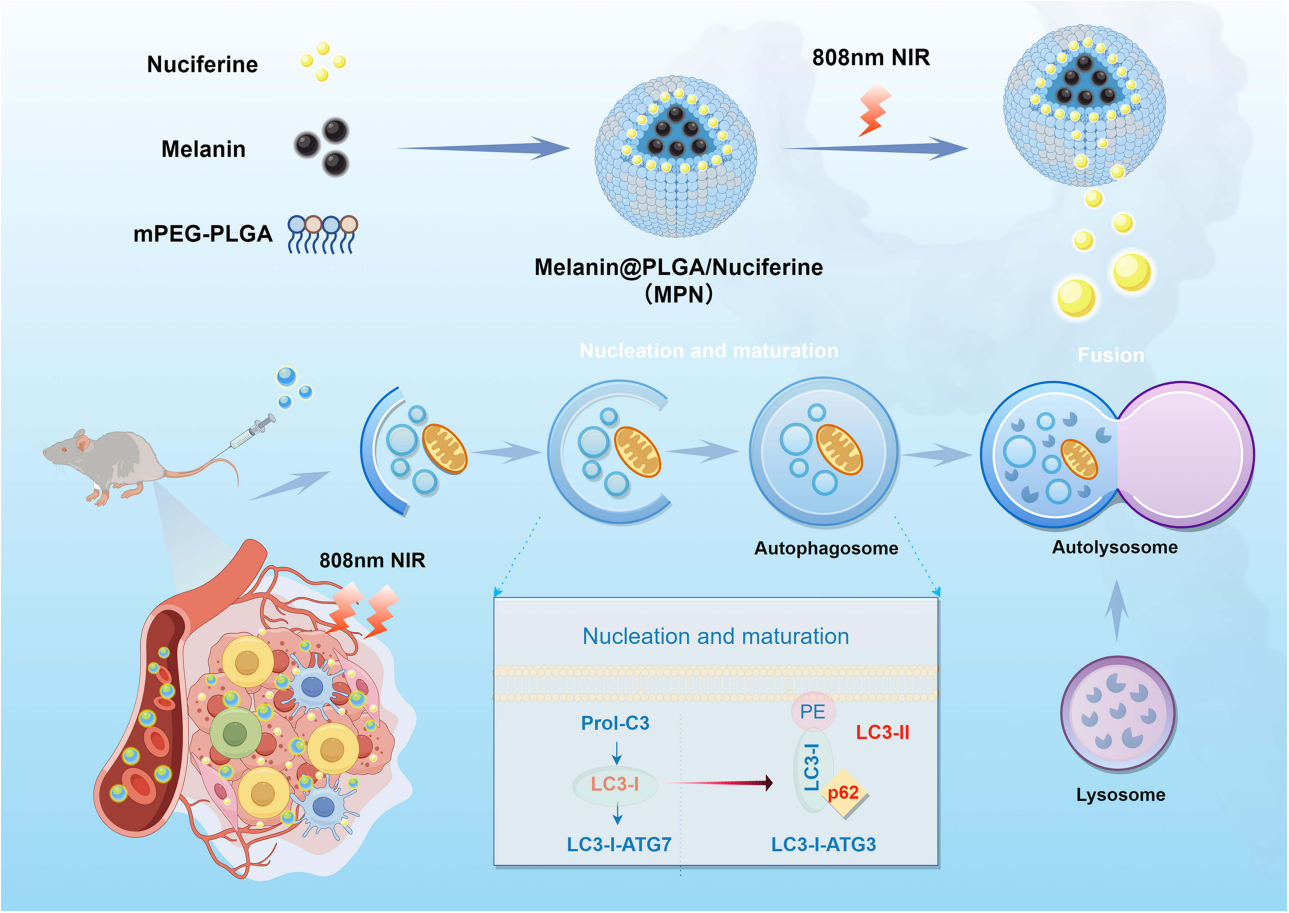

the body and the associated adverse effects. Furthermore, Mel has magnetic resonance imaging (MRI) properties that improve the visibility of tumor lesions in T1-weighted MR images, facilitating precise applications of PTT.[14]

Recent studies on PTT have indicated that the degree of PTT must be strictly controlled. Excessive PTT can cause damage to the healthy tissue surrounding the tumor, whereas mild PTT can induce protective autophagy in tumor cells, allowing them to evade destruction.[15,16] Autophagy plays a dual role: moderate autophagy activates self-protection mechanisms to cope with damage or stress, whereas excessive autophagy may lead to autophagic cell death.[17,18] Therefore, precisely controlling PTT while inhibiting the protective autophagy of tumor cells or promoting the over-activation of autophagy in tumor cells may represent a novel strategy to increase the efficacy of PTT. Nuciferine (NF), a compound derived from lotus leaves, has important pharmacological properties and can inhibit tumor cell proliferation by inducing autophagy with minimal side effects.[19] Therefore, combining NF with the thermal stress induced by PTT may promote the overactivation of autophagy in tumor cells, thereby improving the effectiveness of PTT.

Owing to the stable and safe performance, poly (lactic acid-co-glycolic acid) (PLGA) copolymer has been commercialized for drug delivery in the controlled-release field.[20] In this study, we utilized the PLGA as a carrier to encapsulate Mel and NF for the formulation of melanin@PLGA/nuciferine (MPN) nanoparticles. MPN served as both a photothermal conversion agent and an imaging agent, accumulating in tumor tissues by exploiting the enhanced permeability and retention effect, thus facilitating the localization of HCC cells via MRI. Upon NIR irradiation, the release of NF from the PLGA shell via PTT stimulated autophagy in tumor cells, leading to autophagic cell death and thereby enhancing the overall effectiveness of PTT for eradicating HCC.

Materials and Methods

Cells and Reagents

Huh7 and HCCLM3 cells were obtained from the Institute of the Chinese Academy of Sciences, while HepG2 hepatoma cells were obtained from the American Type Culture Collection. All cells were cultivated in Dulbecco's modified Eagle's medium (DMEM) supplemented with 10% fetal bovine serum and 1% penicillin–streptomycin and maintained in a 5% CO_2 atmosphere at 37°C. mPEG5000-PLGA (MW: 15 kDa), dichloromethane, poly (vinyl alcohol) (PVA, 99% purity, MW: 30–70 kDa) and isopropanol were supplied by Chongqing East Chemical Industry. NF and Mel were obtained from Avanti Research Co. and Sigma–Aldrich, respectively.

MTT Assay

Cells were seeded in 96-well plates at a density of 7×10^5 cells per well, with 5–6 replicate wells per treatment group. Serial dilutions of NF or different nanoparticle suspensions (200 μL/well) were added and incubated for 24 h or 48 h. To assess the effect of the nanoparticles on cell viability with and without NIR irradiation, the respective wells in the irradiation group were exposed to 808 nm NIR light (1.5 W/cm^2) for 5 minutes following treatment addition. After incubation, 20 μL of MTT solution was added (20 μL/well), followed by further incubation in the dark for 4 hours. The supernatant was then carefully aspirated, and dimethyl sulfoxide (DMSO; Sigma–Aldrich, St. Louis, MO, USA) was added to solubilize the formazan crystals at room temperature for 15–30 minutes. Cell viability was assessed by measuring the optical density (OD) of each well with a microplate reader (BioTek, Vermont, US) at 490 nm.

Western Blotting Analysis

Protein was extracted from Huh7 and HepG2 cells with a complete lysis method. The protein concentration was determined via the bicinchoninic acid (BCA) assay. Equal masses of protein samples were loaded into the wells of a gel for electrophoresis, and subsequently, the proteins were transferred to a nitrocellulose (NC) membrane for Western blotting. Following complete blockade of the protein bands, appropriate concentrations of antibodies against beclin-1, p62, LC3, and GAPDH (1: 1000, obtained from Proteintech Group, Wuhan, China) were applied for incubation overnight at 4°C. After thorough washing, the samples were incubated with the corresponding rabbit/mouse fluorescent secondary antibodies for 1–2 hours in the dark. The blots were scanned and analyzed with the Odyssey fluorescence imaging system (LI-COR Biosciences, Nebraska, USA), and the intensities of the bands were quantitatively assessed via ImageJ software. The experiment was repeated 3 times.

Monodansylcadaverine (MDC) Staining

MDC is an autofluorescent dye that is capable of labeling autophagosomes. In accordance with published procedures, Huh7 cells were centrifuged at 800 × g for 5 minutes and washed with 400 μL of washing buffer.[21] Subsequently, 90 μL of the cell suspension (1×10^5 cells/mL) was transferred into an Eppendorf (Ep) tube, and 10 μL of 0.05 mM MDC staining solution (Solarbio, Beijing, China) was added and gently mixed. Huh7 cells were stained for 30 minutes in the dark, after which they were centrifuged and subjected to another washed. Then 100 μL of collection buffer was added to each Ep tube for resuspending the cells. Finally, cells were smeared onto slides and examined via confocal laser scanning microscopy (CLSM) (BX53, Olympus, Japan), utilizing excitation light at 355 nm and blocking light at 512 nm.

Preparation of MPN

MPN (Mel@PLGA/NF), MP (Mel@PLGA), and PN (PLGA/NF) were synthesized via the double emulsion method.[22] PLGA (50 mg) and NF (4 mg) were dissolved in 4 mL of dichloromethane. Following complete sonication, 400 μL of melanin (Mel) solution (15 mg/mL, neutralized to pH 7.5) was added dropwise. The mixture was emulsified by sonication. Subsequently, 8 mL of PVA solution (4% w/v) and 10 mL of isopropanol solution (2% v/v) were added sequentially and mixed thoroughly. The resulting emulsion was transferred to a beaker and stirred magnetically for 3 hours to allow solvent evaporation. The particles were then collected by centrifugation and after washing were

resuspended with 4 mL of deionized water to yield the MPN suspension. MP: Synthesized identically to MPN but without the addition of NF. PN: Synthesized identically to MPN but with deionized water replacing the melanin solution.

Characterization of MPN

The overall morphology of MPN was assessed using light microscopy (Olympus, Japan). For detailed structural analysis, MPN suspension was deposited onto a copper foil grid and examined by transmission electron microscopy (TEM, Hitachi H-7600, Japan). The particle size distribution and zeta potential of MPN were measured using the Zetasiser analyzer (Malvern, UK). To evaluate colloidal stability, MPN was suspended in DMEM supplemented with 10% fetal bovine serum. Changes in particle size were monitored over 15 days after preparation. Ultraviolet-visible (UV-Vis) spectrophotometry (scanning range: 200–1000 nm) was employed to obtain the absorption spectra of Mel, NF, and MPN. The encapsulation efficiency and drug loading capacity of the MPN for both NF and Mel were calculated using established formula.[23]

Drug Release of MPN in vitro

The release of NF from MPN, both with and without NIR irradiation, was studied using a centrifugation-based method as previously reported.[24] Following synthesis and washing, MPN was resuspended in 2 mL of PBS containing 0.1% (w/w) Tween-80 and maintained at 37°C. For the NIR-irradiated group, suspensions were exposed to an 808 nm laser (1.5 W/cm²) for 5 minutes prior to sampling. At predetermined time points (0, 4, 6, 12, 24, 48, 72, 96, and 120 h), a 500 μL aliquot of the suspension was collected and centrifuged (15,000 rpm, 10 min). The NF content released into the supernatant was quantified by UV spectrophotometry at 270 nm.

Photothermal Properties of MPN in vitro

To evaluate the photothermal conversion efficiency and stability of MPN, suspensions/solutions of deionized water, PLGA nanoparticles, MP, MPN, and Mel were irradiated with 808 nm NIR light (1.5 or 2.0 W/cm²). The temperature changes were recorded in real-time.

Photothermal stability was assessed by subjecting MPN suspension in a quartz tube to five consecutive irradiation-cooling cycles: 5 minutes of NIR exposure (1.5 or 2.0 W/cm²) followed by minutes of passive cooling. The temperature profiles throughout the cyclic treatment were monitored with a thermal imaging camera (FLIR Systems, USA).

Reactive Oxygen Species (ROS) Detection in vitro

To assess ROS production in Huh7 cells during PTT, we referred to published experimental methods.[25] Cells were divided into six experimental groups: control, NIR (only 808 nm NIR irradiation), NF alone, PN alone, MP + NIR, and MPN + NIR. The groups receiving NIR treatment were irradiated with 808 nm NIR light (1.0 W/cm²) for 5 minutes immediately after nanoparticle addition. Following a 24-hour incubation period postintervention, cells were loaded with the ROS-sensitive fluorescent probe DCFH-DA according to the instructions of the ROS Assay Kit (Beyotime, Shanghai, China) and incubated for 1 hour at 37°C. Intracellular ROS generation was subsequently visualized using the CLSM.

Animals and the Subcutaneous Tumor-Bearing Mouse Model

Male BALB/c nude mice (4–5 weeks, 18–20 g) were obtained from Beijing Vital River Laboratory Animal Technology Co., Ltd. All animal procedures were approved by the Ethics Committee of the First Affiliated Hospital of Harbin Medical University and conducted in accordance with the Declaration of Helsinki and national guidelines for the ethical conduct of biomedical research involving animals.

To establish subcutaneous HCC model, the dorsal skin of the left hind limb was disinfected with 75% ethanol. Subsequently, 200 μL of the Huh7 cell suspension (1×10^6 cells) was injected subcutaneously into the prepared site. Tumor dimensions (length and width) were measured daily using calipers. The tumor volume was calculated as $V = (\text{length} \times \text{width}^2)/2$, and inoculation proceeded until volumes reached approximately 150 mm³.

PTT for Tumors in vivo

HCC tumor-bearing mice were randomly assigned to 5 groups (n = 4): (1) saline control (2) NF alone (3) MPN alone (4) MP + NIR and (5) MPN + NIR. All groups received intravenous injections (100 μL) of their respective formulations via tail vein every 48 h for 14 days. The NF, MPN, and MPN + NIR groups were administered equivalent NF doses (2 mg/kg). On day 1, groups 4–5 underwent tumor irradiation with 808 nm NIR light (2 W/cm², 10 min) 6 hours post-injection of MP or MPN suspensions.[22,23]

Tumor volumes and body weights were monitored every other day throughout the treatment period. Growth curves were plotted to evaluate therapeutic efficacy across groups.

MRI Function of MPN

In vitro T1-Weighted MRI Assessment

Suspensions of PLGA, PN, MP, MPN, and a melanin (Mel) solution were prepared. Aliquots (1 mL) of each suspension/solution were dispensed into designated Eppendorf tubes. T1-weighted imaging (T1WI) was performed with a 3.0 T MRI system (Achieva TX, Philips Healthcare, Netherlands) with the following parameters: TR/TE = 515/9.3 ms; FOV = 40 mm × 40 mm × 18 mm; voxel size = 0.3 mm × 0.4 mm × 1 mm; slices = 18; NSA = 5; FA = 90°.

In vivo MRI

Tumor-bearing mice received an intravenous tail vein injection of either saline or the MPN suspension (150 μL). Approximately 6 hours postinjection, the mice were anesthetized and placed within a dedicated mouse quadrature coil. MRI scans were conducted, and comparable image sections (regions of interest) were selected for analysis.

Ultrasound Monitoring of Tumors in vivo

After the tumor-bearing mice were anesthetized, ultrasound evaluations were conducted on the dimensions, vascular perfusion, and tissue rigidity of the subcutaneous tumors using the linear array probe L12–5 (frequency range: 5–12 MHz) of the ultrasound equipment (Aplio500, Japan) provided by Canon Healthcare. This assessment utilized B-mode imaging, color Doppler flow imaging (CDFI), color power angiography (CPA), and elastography (USE) to detect the morphology, size, blood flow, microcirculation within and around the tumor, and stiffness of the tumor separately.

Immunohistochemical (IHC) and Hematoxylin and Eosin (H&E) Staining

Following euthanasia, tumor tissues and major organs were harvested from the tumor-bearing mice. The collected tissues were thoroughly rinsed, dehydrated through a graded ethanol series, cleared in xylene, embedded in paraffin, and sectioned at a thickness of 5 μm. Sections then underwent sequential processing steps: baking, dewaxing, rehydration, antigen retrieval, and blocking. The results were analyzed using ImageJ software.

Tumor sections were immunostained for beclin-1, p62, and LC3. In addition, sections of major organs were stained with hematoxylin and eosin (H&E). All slides were evaluated under the microscope (BX53, Olympus, Japan) at both low and high magnification.

Statistical Analysis and Figure Drawing

Schematic diagrams were created using the Figdraw platform. All statistical analyses were performed using GraphPad Prism software. Parametric comparisons between two groups were assessed using the unpaired *t*-test, whereas differences among multiple groups were evaluated using one-way analysis of variance (ANOVA). A *p*-value of less than 0.05 ($p < 0.05$) was considered statistically significant for all analyses.

Results

NF Inhibited the Viability of HCC in vitro

MTT assays revealed that NF significantly reduced the viability of Huh7, HCCLM3, and HepG2 cells in a concentration-dependent manner (Figure 1A–C). Notably, the inhibitory effect of NF on Huh7 cells was consistently stronger than that

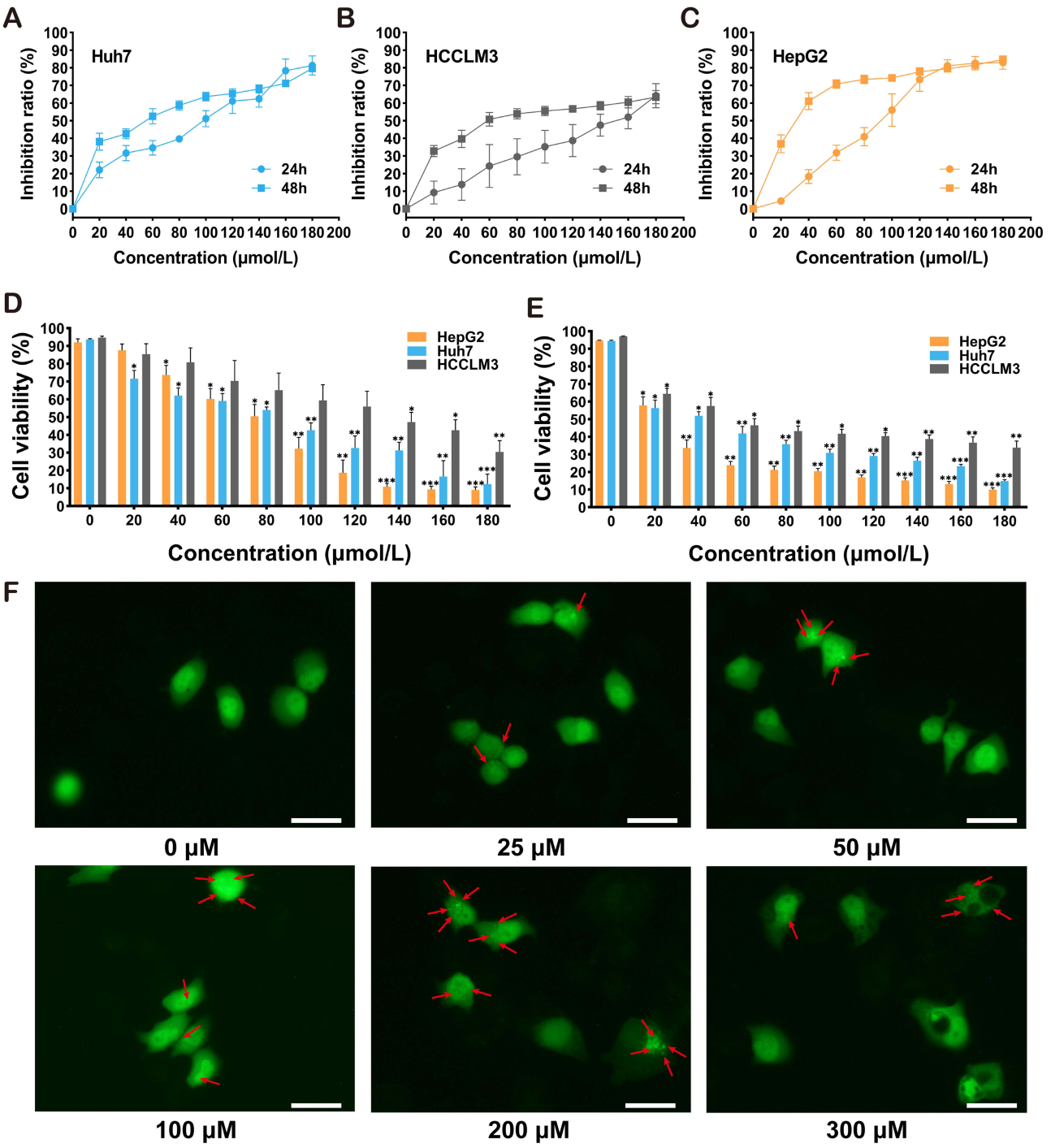

Figure 1 NF inhibited the viability and induced autophagosome formation of HCC in vitro. Cell viability inhibition rates of (**A**) Huh7, (**B**) HCCLM3 and (**C**) HepG2 cells treated with NF. Cell viability of Huh7, HCCLM3 and HepG2 cells treated with NF for (**D**) 24 h and (**E**) 48 h. (**F**) Representative CLSM images (400×) showing MDC-stained autophagosomes in Huh7 cells treated with increasing concentrations of NF. Arrows indicate autophagosomes, scale bar = 25 μm. *$p < 0.05$, **$p < 0.01$, ***$p < 0.001$.

on HCCLM3 cells. Furthermore, the inhibitory effect after 48 h of NF treatment was more pronounced than that observed after 24 h (Figure 1D–E).

MDC staining revealed that the number of autophagosomes in Huh7 cells increased with escalating NF concentrations. However, at the highest concentration tested (300 μM), morphological alterations occurred, leading to compromised cellular structural integrity and a consequent reduction in autophagosome formation in Huh7 cells (Figure 1F).

NF Promoted Autophagy in HCC in vitro

Western blot analysis further demonstrated that 24-hour NF treatment of HepG2 and Huh7 cells induced a concentration-dependent increase in the expression of beclin-1, a key regulator of classical autophagy initiation. Moreover, the LC3-II/LC3-I ratio, which is indicative of autophagosome formation and elongation, also increased. However, the expression of p62, a protein essential for autophagic cargo degradation, did not significantly change (Figure 2A–C). Following 48 h of NF treatment, p62 expression decreased progressively with increasing NF concentrations. Moreover, the increase in the LC3-II /LC3-I ratio remained positively correlated with NF concentration and was more pronounced than at the 24-hour time point. In contrast, beclin-1 expression was not significantly altered (Figure 2D–F). Notably, the PI3K inhibitor 3-MA failed to inhibit the autophagy-promoting effect of NF (Figure 2G and H).

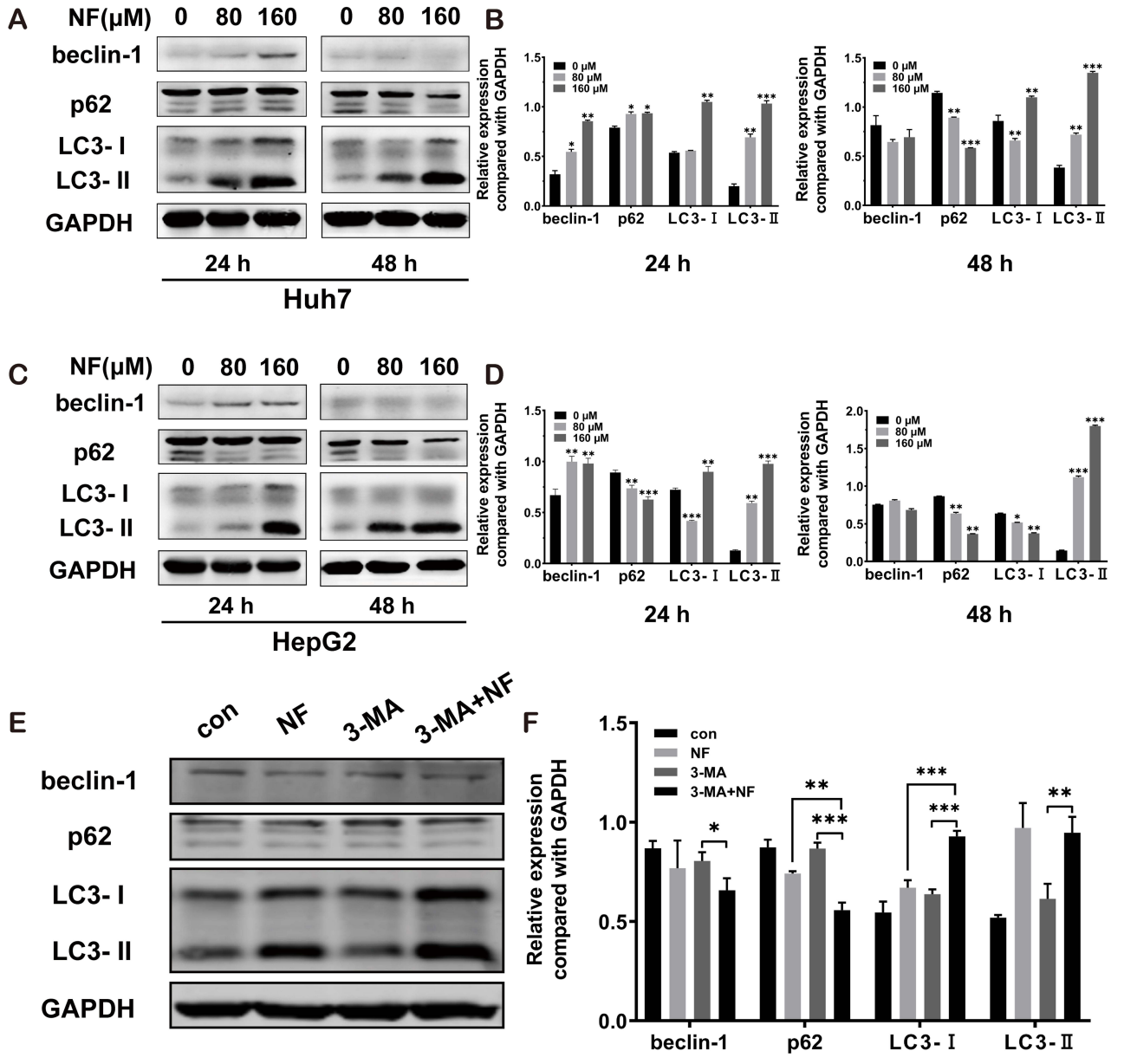

Figure 2 NF triggered autophagy in Huh7 and HepG2 cells. (**A**) Western blotting analysis of beclin-1, p62, and LC3 in Huh7 cells treated with NF. (**B**) Relative expression levels of beclin-1, p62, LC3-I, and LC3-II normalized to GAPDH in Huh7 cells treated with NF for 24 h and 48 h. (**C**) Western blotting analysis of beclin-1, p62, and LC3 in HepG2 cells treated with NF. (**D**) Relative expression levels of beclin-1, p62, LC3-I, and LC3-II normalized to GAPDH in HepG2 cells treated with NF for 24 h and 48 h. (**E**) Representative Western blotting analysis of beclin-1, p62, LC3-I, and LC3-II protein levels in Huh7 cells co-treated with 120 μM NF in the presence or absence of 5 mM 3-MA for 6 h. (**F**) Relative protein expression levels (normalized to GAPDH) of beclin-1, p62, LC3-I, and LC3-II in Huh7 cells under the treatment conditions described in (E). *$p < 0.05$, **$p < 0.01$, ***$p < 0.001$.

https://doi.org/10.2147/IJN.S536620

Characterization and Stability of MPN

MPN and other nanoparticles were synthesized, freeze-dried, and stored for subsequent experiments (Figure 3A). The MPN suspension in PBS solution is shown (Figure 3B). Transmission electron microscopy (TEM) revealed that the MPN particles were spherical, well-dispersed, and appeared black (electron-dense) (Figure 3C). Higher magnification imaging (above 10,000×) showed a homogeneous black core surrounded by a transparent, ring-shaped outer shell approximately 15 nm thick (Figure 3D–E). MPN had an average diameter of 295.3 ± 23.3 nm, with a zeta potential of −17.5 ± 0.6 mV (Figure 3F and G). Within 15 days after preparation, the average particle size of MPN did not show significant change as detected by the size analyzer (Figure 3H).

Drug Loading and Release Properties of MPN

The absorbance of Mel gradually decreased with increasing wavelength, whereas NF exhibited a specific absorption peak at 270 nm (Figure 4A and B). The UV spectrum of MPN displayed characteristic absorption features of both NF and Mel, confirming successful synthesis (Figure 4C). At wavelengths above 400 nm (outside the absorption range of NF), the PLGA absorbance remained below 0.1, while Mel continued to absorb. Standard curves and linear regression

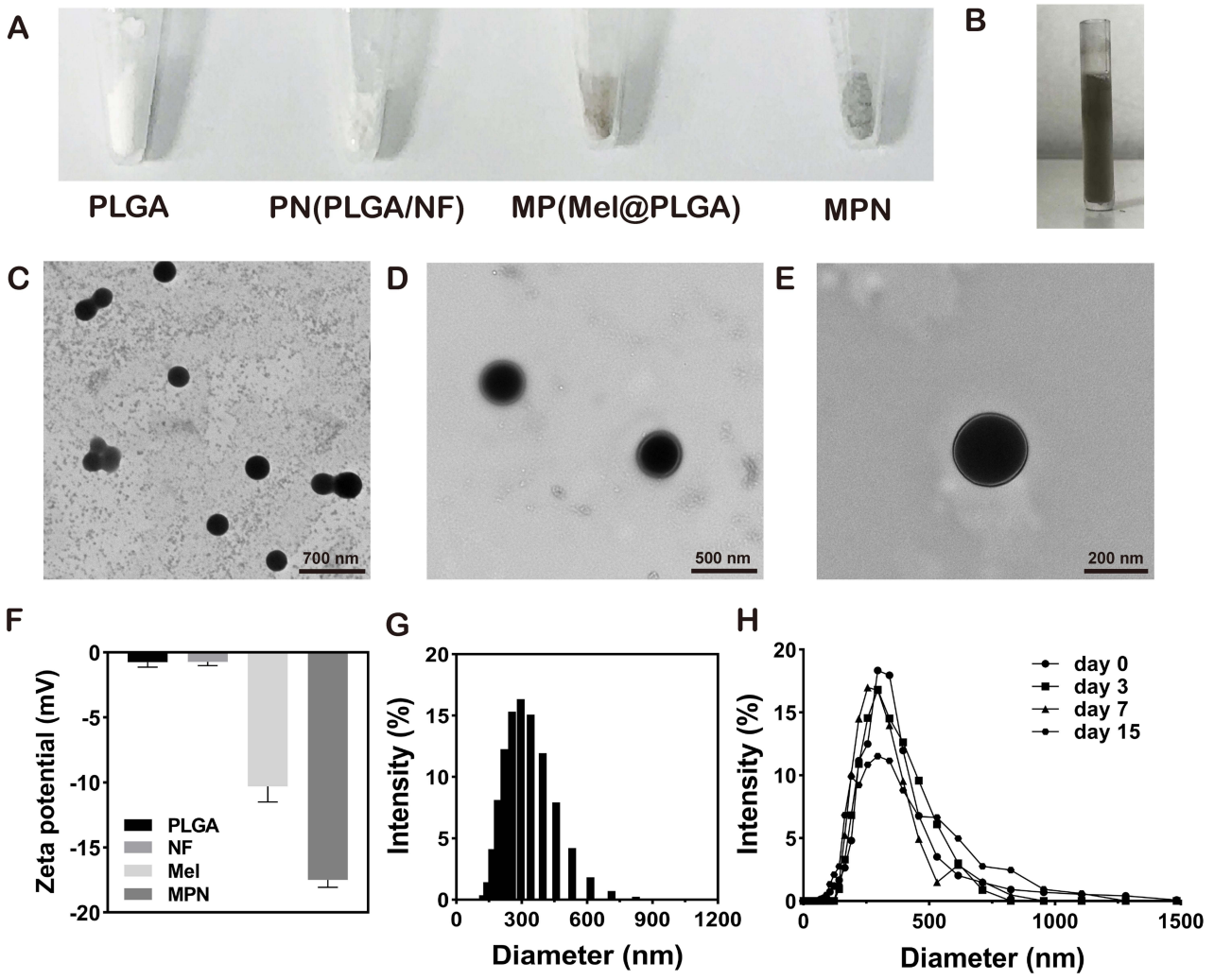

Figure 3 Characterization of MPN. (**A**) Lyophilized powders of PLGA, PN, MP, and MPN nanoparticles. (**B**) The MPN suspension placed in a quartz tube. (**C**) The TEM image of MPN under 7.0k magnification, scale bar = 700 nm. (**D**) The TEM image of MPN under 10.0k magnification, scale bar = 500 nm. (**E**) The TEM image of MPN under 25.0k magnification, scale bar = 200 nm. (**F**) The Zeta potential of PLGA, NF, Mel and MPN. (**G**) The size distribution and (**H**) size changes during 15 days after preparation of MPN.

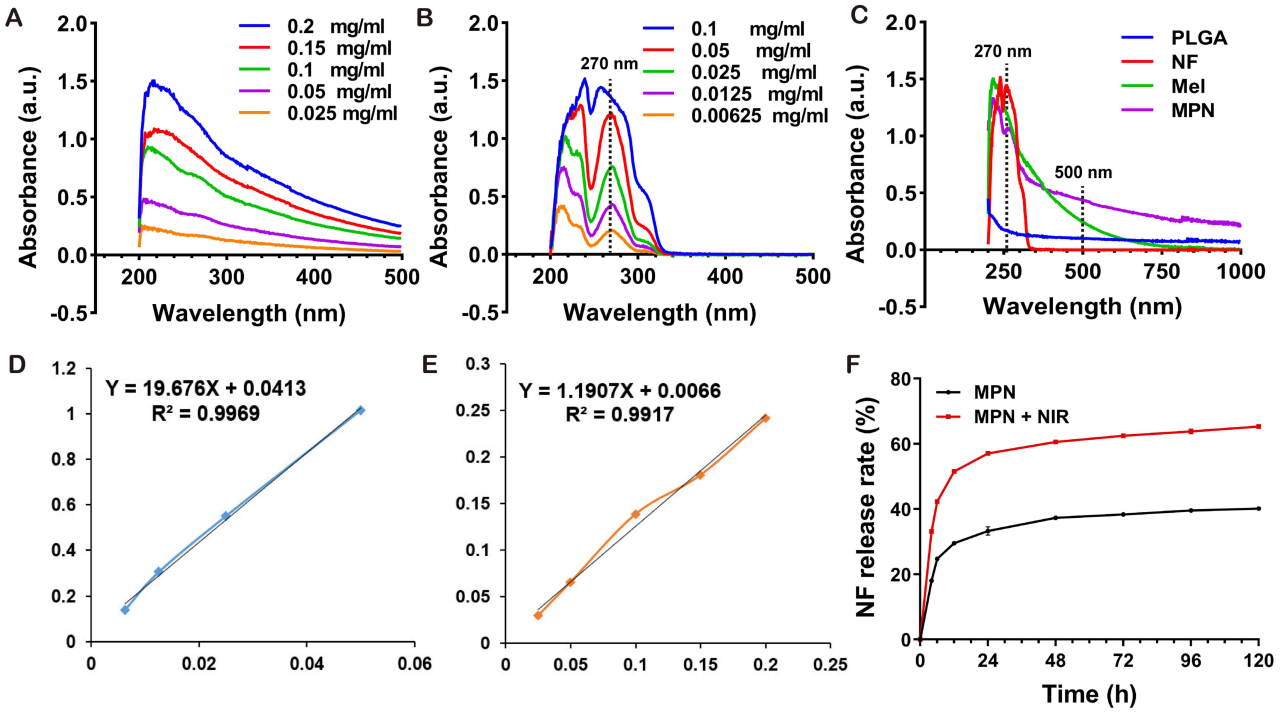

Figure 4 The drug loading and release ability of MPN. UV spectra of (**A**) Mel and (**B**) NF in gradient concentrations. (**C**) UV spectra of PLGA, NF, MPN and Mel. The drug standard curves and the linear regression equations of (**D**) Mel and (**E**) NF. (**F**) The release rate of NF from MPN under the presence or absence of 808 nm NIR irradiation.

equations for Mel and NF were established using UV–Vis spectroscopy: Mel: Y = 1.190X + 0.006, R^2 = 0.991; NF: Y = 19.67X + 0.041, R^2 = 0.996 (Figure 4D and E). Leveraging the distinct absorption profiles of Mel (at 500 nm) and NF (at 270 nm), the drug loading content (DLC) and encapsulation efficiency (EE) for each drug within the MPN were calculated. The EE and DLC for Mel were 86.2 ± 2.6% and 41.2 ± 0.4%, respectively. For NF, the EE was 33.1 ± 9.9% and that of DLC was 8.2 ± 1.5%. Given the specific focus of this study on the pharmacological activity of NF within the MPN, in vitro drug release experiments were conducted to assess NF release from the MPN with or without NIR irradiation. Without NIR irradiation, the cumulative NF release reached 40.2%. In contrast, under NIR irradiation, the release significantly increased to approximately 65.3% (Figure 4F).

Photothermal Performance of MPN in vitro

The results indicated that there was no significant temperature change in either the PLGA suspension or the deionized water under NIR irradiation. In contrast, the temperatures of both the MP and MPN suspensions increased progressively with irradiation time. Following 5 minutes of irradiation at 1.5 W/cm², the Mel solution temperature rose by 29.1°C, while the MPN suspension temperature increased by 16.0°C (Figure 5A). At a higher power density of 2.0 W/cm² for 5 minutes, the Mel solution temperature increased by 40.8°C, and the MPN suspension temperature increased by 19.8°C (Figure 5B).

Furthermore, the photothermal stability of the MPN suspension was evaluated through periodic NIR irradiation (808 nm, 1.5 W/cm² or 2.0 W/cm²). Notably, no significant decrease in photothermal activity was observed over 5 cycles, demonstrating the favorable photothermal stability of MPN (Figure 5C and D). To evaluate the cytotoxicity of PLGA, PN, MP, MPN, and Mel on Huh7 cells with or without NIR irradiation (1.5 W/cm²), MTT assays were performed. The concentration of Mel solution was set to 2 mg/mL based on the DLC of MPN. Specifically, MPN alone reduced Huh7 cell viability to 63.01% (Figure 5E). NIR irradiation substantially amplified the cytotoxic effect of MPN, further decreasing average cell viability to 36.45% (Figure 5F). Results confirmed that neither PLGA nor PN exhibited responsiveness to NIR irradiation. However, when combined with NIR, Mel, MP, and MPN significantly reduced cell viability, demonstrating the in vitro PTT effect (Figure 5G). Furthermore, MPN exhibited a stronger inhibitory effect on cell viability than MP, irrespective of irradiation. Although MP demonstrated superior photothermal heating capability compared to MPN, the combined effect of MPN + NIR

https://doi.org/10.2147/IJN.S536620

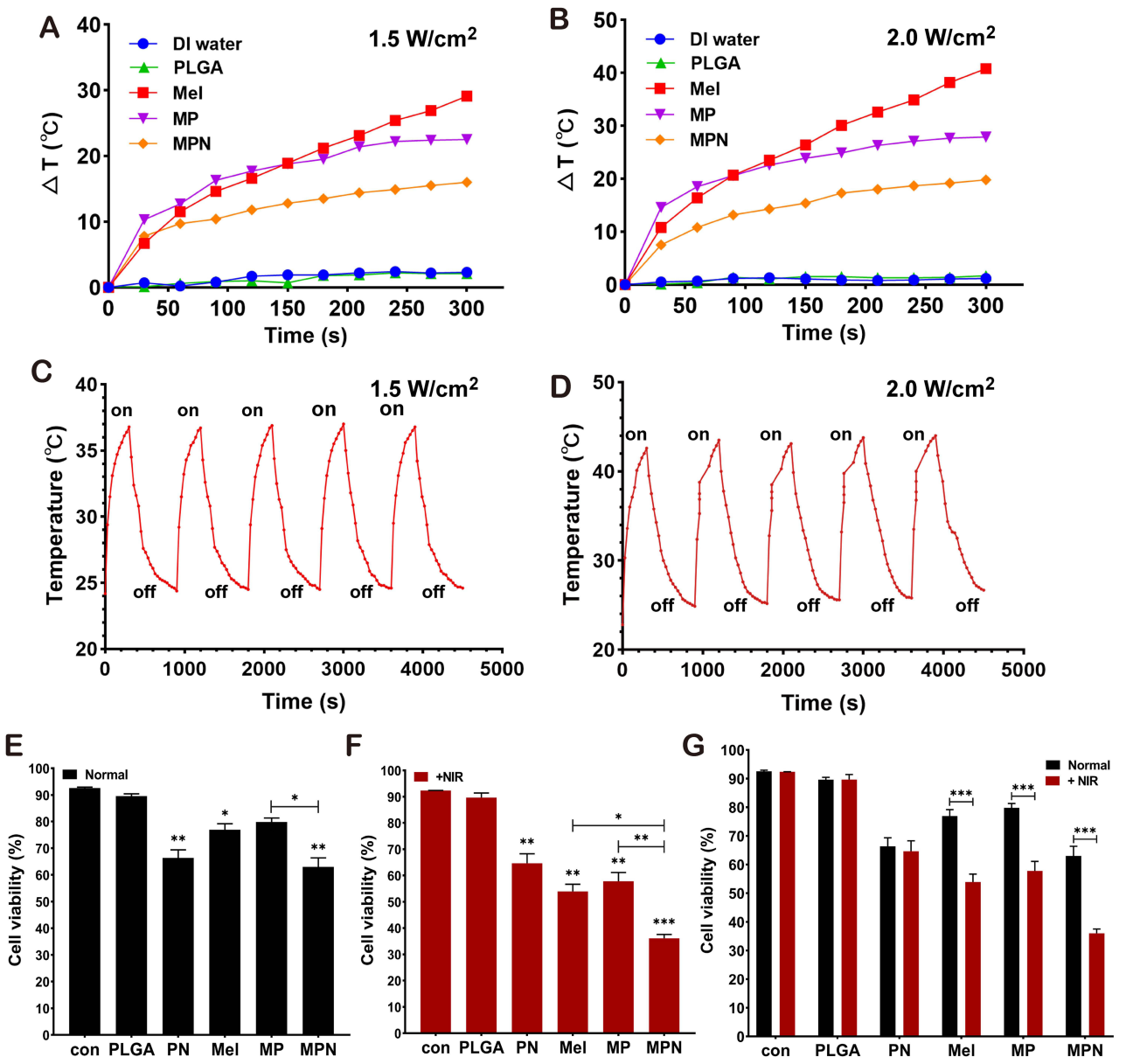

Figure 5 Photothermal performance of MPN in vitro. The temperature variation of PLGA, MP, MPN suspensions and Mel solution irradiated with (**A**) 1.5 W/cm² and (**B**) 2.0 W/cm² 808 nm NIR for 5 minutes. Temperature variation curves under periodic irradiation of MPN suspension for 5 cycles at (**C**) 1.5 W/cm² and (**D**) 2.0 W/cm² with 808 nm NIR. Effects of PLGA, PN, MP, MPN and Mel on the viability of Huh7 cells (**E**) with or (**F**) without 808 nm NIR irradiation (1.5 W/cm², 5 min). (**G**) Overall analysis of the inhibitory effect of PTT groups on the viability of Huh7 cells. $p < 0.05$, $^{**}p < 0.01$, $^{***}p < 0.001$.

was significantly more potent than that of MP + NIR. This enhanced efficacy is likely attributable to the release of NF from MPN and the subsequent exertion of its pharmacological activity.

MPN + NIR Further Promoted Autophagy in HCC in vitro

To elucidate the potential mechanism by which NF enhances PTT, we measured intracellular ROS levels in Huh7 cells. As shown in CLSM images (Figure 6A), 808 nm NIR irradiation alone, in the absence of photothermal agents, had no effect on either cell viability or intracellular ROS levels. Treatment with NF or MPN alone significantly decreased cell viability and induced morphological changes, but did not trigger detectable ROS production. In contrast, both the MP + NIR and the MPN + NIR groups exhibited the increase in ROS, the fluorescence intensities of these two irradiated groups were similar.

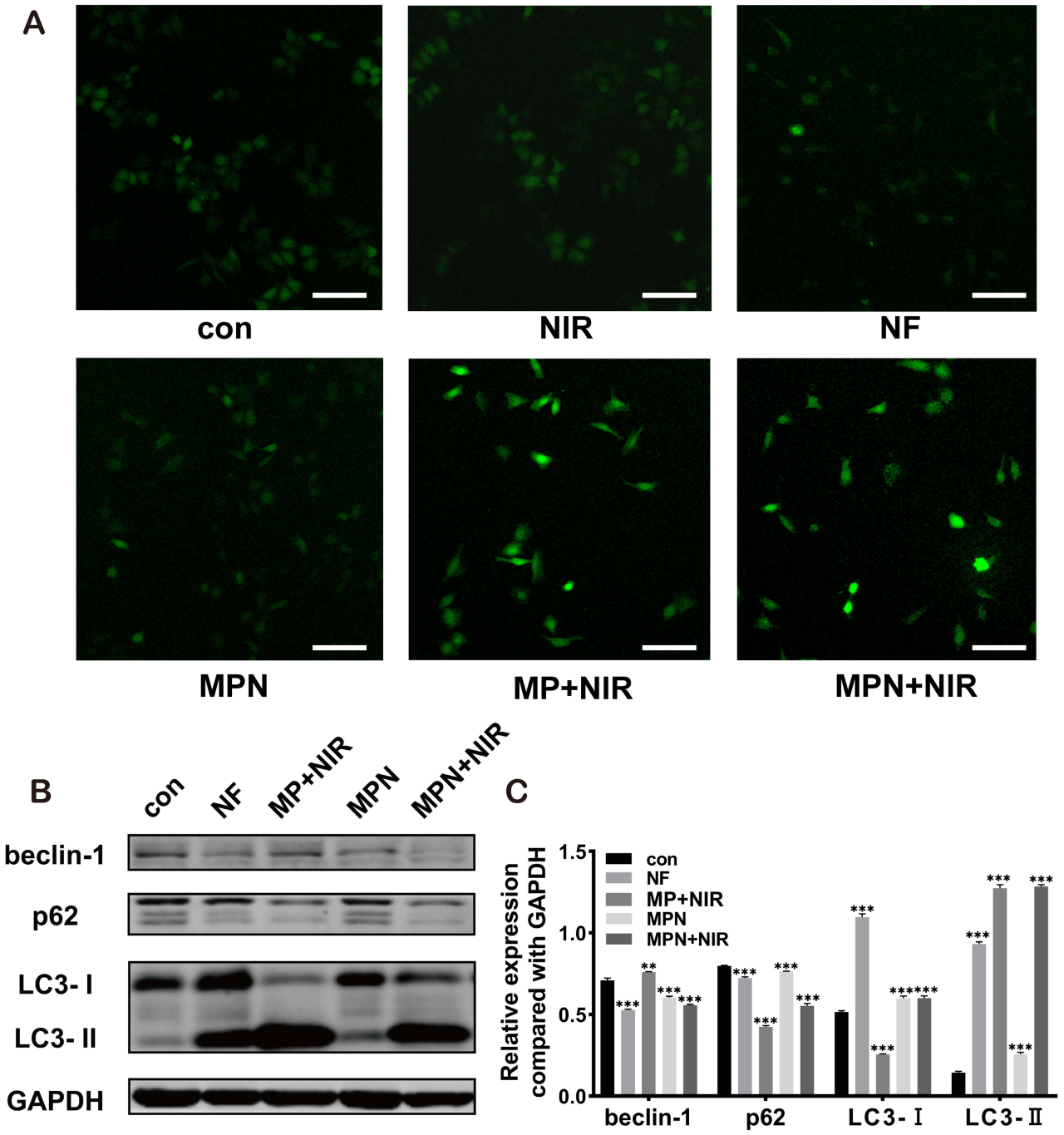

Figure 6 The mechanism analysis of MPN-mediated PTT in vitro. (**A**) CLSM images (100×) of ROS in Huh7 cells. The intensity of green fluorescence in the Huh7 cells represented the amount of ROS, scale bar = 100 μm. (**B**) Western blotting and (**C**) the relative expression levels (normalized to GAPDH) of beclin-1, p62 and LC3 in Huh7 cell. $^{**}p < 0.01$, $^{***}p < 0.001$.

To further investigate the underlying mechanisms involved in autophagy, Huh7 cells were divided into 5 groups: control, NF, MPN, MP + NIR, and MPN + NIR. Due to the limited emission range of the NIR laser probe preventing uniform irradiation, water bath heating was employed to replicate the thermal profiles induced by 1.5 W/cm² NIR irradiation for 5 minutes. The temperature was set at 59.5°C for the MP + NIR group and 53°C for the MPN + NIR group, consistent with prior in vitro photothermal conversion results.

https://doi.org/10.2147/IJN.S536620

Analysis of autophagy markers revealed that MP + NIR (PTT alone) decreased the expression of beclin-1 and p62 while increasing LC3 lipidation (Figure 6B). Comparatively, MPN + NIR irradiation further enhanced LC3-I expression, attributable to the presence of NF. Additionally, elevated overall LC3 expression and increased LC3-II conversion (indicative of LC3-I to LC3-II processing) were detected in both the NF and MPN groups (Figure 6C).

MPN Enhanced the MRI Signal Intensity

Suspensions of PLGA, PN, MP, MPN, and a melanin (Mel) solution were prepared for T1-weighted MRI assessment. Compared to deionized water, the signals of PLGA and PN suspensions were negligible. In contrast, MP and MPN suspensions showed significantly greater signal intensities, although these intensities were lower than that of the Mel solution (Figure 7A). Approximately 6 hours post-injection of either saline or the MPN suspension via the tail vein into tumor-bearing mice, T1-weighted imaging (T1WI) revealed a scattered distribution of high signal intensity within the tumors of the MPN group (Figure 7B). This confirmed the successful accumulation of MPN at the tumor site, thus permitting enhanced visualization of the tumor lesions.

MPN + NIR Ablated the Tumor and Inhibited HCC Progression

The in vivo treatment plan lasts 14 days, and ultrasound was used to monitor the tumor size and other features (Figure 7C). Approximately 6 hours post-administration of MPN to tumor-bearing mice via the tail vein, tumors were irradiated with 808 nm NIR light (2.0 W/cm², 10 min). We observed the tumors in the PTT groups. Immediately after irradiation, scattered hemorrhagic spots and surrounding skin edema were observed. On day 1 posttreatment, the tumor epidermis exhibited necrosis. By day 7, the necrotic tissue showed signs of organization, accompanied by a marked reduction in tumor volume. By day 14, eschar detachment indicated partial tumor ablation (Figure 7D).

Ultrasound assessments performed during treatment across all groups revealed that NF or MPN alone delayed tumor progression, resulting in slight decreases in tumor vascular density and stiffness. In contrast, the groups receiving MP + NIR and MPN + NIR demonstrated varying degrees of tumor ablation, leading to pronounced reductions in vascular density and stiffness. Notably, the MPN + NIR group exhibited the strongest effect (Figure 7E).

Tumor-bearing mice in each group underwent their respective treatments for 14 days. Upon complete tumor excision, a visual comparison of tumor sizes across groups was conducted (Figure 7F). Additionally, mouse body weights ranged from 22–28 g, with no significant intergroup differences (Figure 7G). NF treatment only delayed tumor progression, whereas MPN monotherapy inhibited tumor growth. In the PTT groups (MP + NIR and MPN + NIR), tumors were effectively ablated and the MPN + NIR group showed a significant reduction in tumor volume (Figure 7H).

MPN + NIR Promoted Autophagy in HCC in vivo

To further investigate whether MPN + NIR can enhance the therapeutic effect of PTT by influencing autophagy, we conducted immunohistochemical staining on the tumor tissues after treatment (Figure 8A). IHC analysis of HCC tumor tissues demonstrated that MPN + NIR treatment significantly reduced beclin-1 and p62 expression concomitantly with a substantial iincrease in LC3 expression (Figure 8B).

The biological safety of nanoparticles is crucial for their use as therapeutic agents. Therefore, we performed H&E staining on major organs from tumor-bearing mice. Images of major organs revealed no treatment-induced pathological damage, particularly in the liver and kidneys, indicating favorable biosafety of the MPN in vivo (Figure 8C).

Discussion

In this study, we developed melanin@PLGA/nuciferine (MPN) nanoparticles leveraging the MRI and photothermal properties of Mel for tumor localization and PTT. Upon thermal activation, NF was rapidly released from MPN. This release promoted autophagosome formation and autophagic flux in tumor cells via PTT-induced autophagy, thereby enhancing PTT efficacy.

PTT represents a novel noninvasive therapeutic approach utilizing nanocarriers for targeted tumor thermal ablation. However, a major limitation is the induction of cytoprotective autophagy in tumor cells.[26,27] Consequently, strategies targeting this cytoprotective autophagy have emerged to improve PTT outcomes. Notably, while numerous studies have

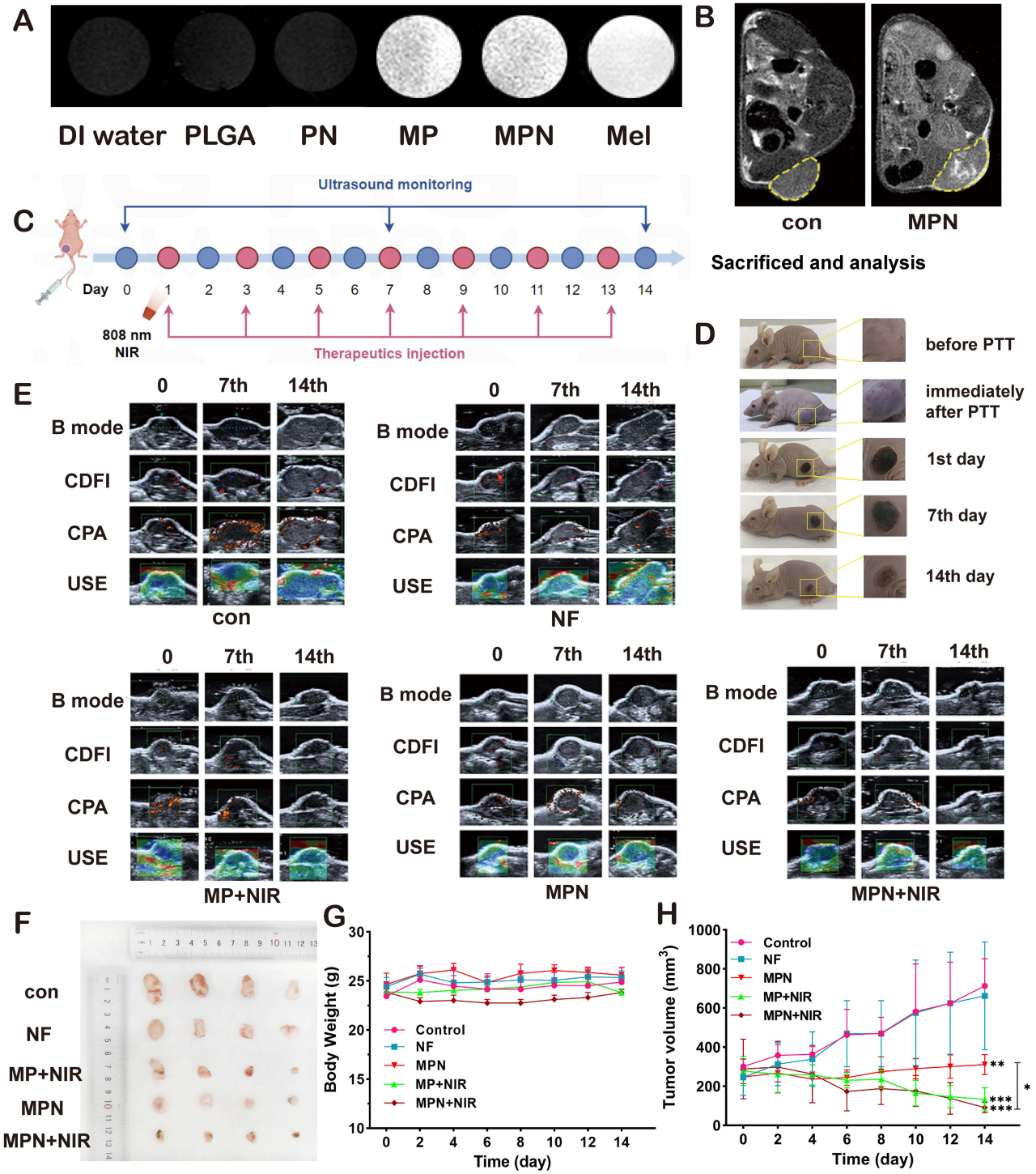

Figure 7 MPN-mediated PTT ablated HCC in vivo. (**A**) T1-weighted MRI images of PLGA, PN, MP, MPN suspensions and Mel solution. (**B**) T1-weighted MRI images of tumors 6 hours post-injection of saline or MPN suspension via the tail vein. The area outlined in yellow is a subcutaneous tumor. (**C**) Schematic diagram illustrating the intracellular treatment mechanism. (**D**) Photographs of subcutaneous tumors before and within 14 days after MPN injection combined with 808 nm NIR irradiation (2.0 W/cm², 10 min) for PTT. The yellow frame highlights the subcutaneous tumor area in the tumor-bearing mouse, with a magnified view shown. (**E**) Multimodal ultrasound imaging (including B-mode, CDFI, CPA and USE) of subcutaneous tumors in each group during the treatment period. (**F**) Photographs of excised tumors from each group on day 14 post-treatment. (**G**) Tumor volume curves and (**H**) body weight curves of tumor-bearing mice in each group over the 14-day treatment period. *$p < 0.05$, **$p < 0.01$, ***$p < 0.001$.

demonstrated that inhibiting autophagy can significantly enhance antitumor therapies, others have indicated that excessive autophagy activation can also induce tumor cell death.[28–33] Given that NF possesses established anti-inflammatory and antitumor properties and has been shown to promote autophagy in melanoma cells,[19,34] we investigated its impact on

https://doi.org/10.2147/IJN.S536620

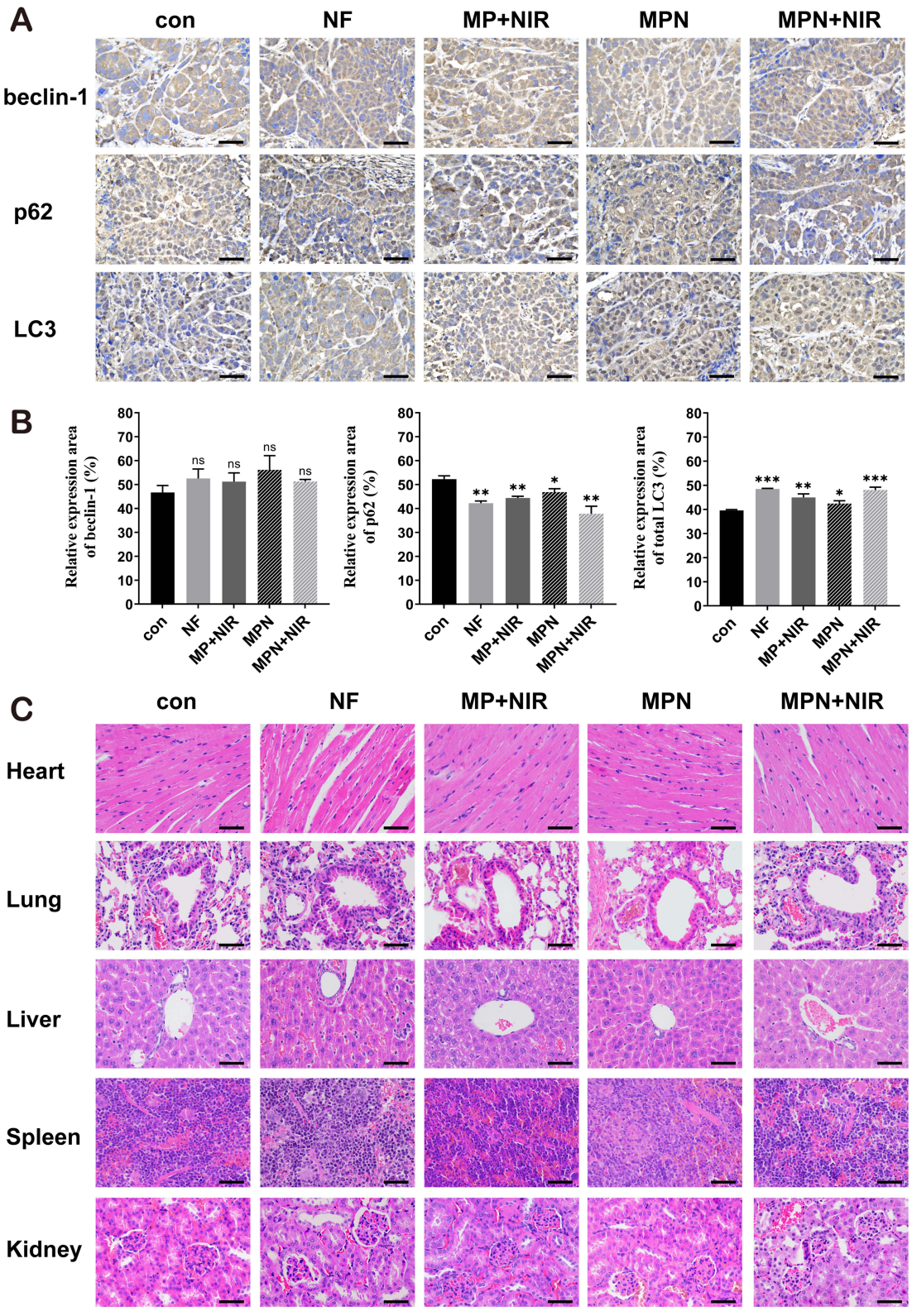

Figure 8 MPN combined with NIR irradiation promoted autophagy of HCC with excellent biocompatibility in vivo. (**A**) Beclin-1, p62 and LC3 immunohistochemical staining of tumor tissues in each group, scale bar = 100 μm. (**B**) The relative expression area of beclin-1, p62 and LC3 of tumor in each group. ns represents no significance. (**C**) H&E staining images of major organs in each group after different treatments, scale bar = 100 μm. *$p < 0.05$, **$p < 0.01$, ***$p < 0.001$.

the viability and autophagy in HCC cells. To ensure comprehensive and reliable results, we initially selected well-established HCC cell lines (Huh7 and HCCLM3), along with the HepG2 hepatoma cell line to investigate the effects and mechanisms of NF. The HepG2 cell line is commonly employed in studies of HCC drug therapy and metabolism due to its metabolic characteristics are similar to HCC and the absence of p53 gene mutation. Our results indicated that NF effectively inhibited the viability of all three cell lines and promoted autophagic flux in both Huh7 and HepG2 cells. Based on these findings, we proceeded with the more NF-sensitive Huh7 cells for subsequent studies. Results revealed that NF enhances autophagosome formation in HCC cells.

Subsequently, we used PLGA, a polymer with excellent biocompatibility and biodegradability, as a nanocarrier to efficiently encapsulate naturally derived Mel and NF, forming the MPN nanoparticles. The MPN exhibited a negative surface charge, which reduced its susceptibility to phagocytic clearance by the reticuloendothelial system. Additionally, its optimal particle size facilitated accumulation within subcutaneous tumors via the enhanced permeability and retention effect, thereby enhancing the T1-weighted MRI signal in the tumor region.[35,36] In vitro and in vivo experimental results demonstrated that MPN exhibited favorable photothermal properties under NIR irradiation, achieving significant tumor ablation. However, analysis of the experimental outcomes revealed several noteworthy observations. In the experiments in vitro, NF effectively inhibited the viability of HCC cells. Conversely, in the in vivo setting, the NF treatment group only delayed tumor growth and did not achieve a high therapeutic efficacy. In contrast, MPN demonstrated enhanced suppression compared to NF in vivo, which was due to its higher tumor-site accumulation through passive targeting via the size and surface charge dependent enhanced permeability and retention effect.[37] While insufficient NF accumulation in tumor tissue following intravenous administration via the tail vein. Besides, the therapeutic regimen involving NF likely requires a prolonged therapeutic duration and the 14-day treatment period employed in our study may have been insufficient.

Analysis of autophagy-related protein expression confirmed that NF further elevated the levels of these proteins in Huh7 and HepG2 cells in the context of PTT-induced autophagy. Interestingly, neither NF alone nor MPN + NIR treatment significantly altered beclin-1 expression in HCC cells. Beclin-1 is a critical component of the initiation complex (PI3K complex) in the classical autophagy pathway, and studies indicate that autophagy associated with beclin-1 upregulation can exert antitumor effects.[18] However, our subsequent experiments revealed that 3-MA failed to completely abrogate the effects of NF. These findings suggest that NF promotes autophagy in HCC cells via mechanisms independent of the canonical beclin-1-dependent pathway.

The study indicates that induction of ROS-dependent autophagy represents an alternative pathway to enhance PTT efficacy.[38] Based on this finding, we also investigated whether NF enhances PTT efficacy by promoting ROS generation. However, our results revealed that NF did not elevate ROS levels in HCC cells. While PTT itself induced oxidative stress, NF did not further augment ROS production. Thus, neither NF nor MPN stimulated ROS generation in HCC cells, indicating that ROS-related pathways are not involved in their mechanisms of action.

Additionally, recent studies have confirmed that NF alleviates hepatocyte steatosis by activating the TFEB-mediated autophagy-lysosomal degradation pathway,[39] which partially supports our mechanistic hypothesis regarding NF-induced autophagy in HCC cells. Critically, LC3 lipidation (ie, the conversion of LC3-I to LC3-II) is essential for TFEB activation, and MPN + NIR treatment significantly enhances LC3 lipidation.[40] This suggests that MPN + NIR may promote autophagy-lysosomal degradation and potentiate PTT effects through TFEB activation.[41] The rising global prevalence of nonalcoholic fatty liver disease (NAFLD) has substantially increased the NAFLD-related HCC incidence.[42–44] If validated, MPN-based therapy may show enhanced efficacy against NAFLD-associated HCC. Our work constitutes a preliminary exploration of NF and MPN + NIR mechanisms without comprehensive mechanistic validation. These findings warrant further in-depth investigation by our group and other interested researchers.

Conclusion

We successfully synthesized melanin@PLGA/nuciferine (MPN) nanoparticles that demonstrated exceptional photothermal conversion capability. MPN enhanced T1-weighted MRI contrast, enabling precise tumor localization. Furthermore, MPN potentiate PTT efficacy by inducing autophagosome formation and augmenting autophagic flux in HCC cells. This targeted autophagy hyperactivation enhanced thermal ablation outcomes and conferred sustained tumor growth suppression post-PTT.

Abbreviations

HCC, hepatocellular carcinoma; PTT, photothermal therapy; NIR, near-infrared; Mel, melanin; MRI, magnetic resonance imaging; NF, nuciferine; PLGA, poly (lactic acid-co-glycolic acid); MPN, melanin@PLGA/nuciferine; DMEM, Dulbecco's modified Eagle's medium; BCA, bicinchoninic acid; CLSM, confocal laser scanning microscopy; NC, nitrocellulose; PVA, poly (vinyl alcohol); TEM, transmission electron microscopy; UV-Vis, Ultraviolet-visible; DLC, drug loading content; EE, encapsulation efficiency; CDFI, color Doppler flow imaging; CPA, color power angiography; USE, elastography; IHC, immunohistochemical; H&E, hematoxylin and eosin; NAFLD, nonalcoholic fatty liver disease.

Acknowledgments

This project was supported by the National Natural Science Foundation of China (Grant No. 82272000).

Disclosure

The authors report no conflicts of interest in this work.

References

1. Vogel A, Meyer T, Sapisochin G, et al. Hepatocellular carcinoma. *Lancet*. 2022;400(10360):1345–1362. doi:10.1016/S0140-6736(22)01200-4
2. Craig AJ, von Felden J, Garcia-Lezana T, et al. Tumour evolution in hepatocellular carcinoma. *Nat Rev Gastroenterol Hepatol*. 2020;17(3):139–152. doi:10.1038/s41575-019-0229-4
3. Kelley RK, Greten TF. Hepatocellular carcinoma - origins and outcomes. *N Engl J Med*. 2021;385(3):280–282. doi:10.1056/NEJMcibr2106594
4. Kang TW, Rhim H. Recent advances in tumor ablation for hepatocellular carcinoma. *Liver Cancer*. 2015;4(3):176–187. doi:10.1159/000367740
5. Huang A, Yang XR, Chung WY, et al. Targeted therapy for hepatocellular carcinoma. *Signal Transduct Target Ther*. 2020;5(1):146. doi:10.1038/s41392-020-00264-x
6. Ahn KS, Kang KJ. Appropriate treatment modality for solitary small hepatocellular carcinoma: radiofrequency ablation vs. resection vs. transplantation? *Clin Mol Hepatol*. 2019;25(4):354–359. doi:10.3350/cmh.2018.0096
7. Qiu Y, Wu Z, Chen Y, et al. Nano ultrasound contrast agent for synergistic chemo-photothermal therapy and enhanced immunotherapy against liver cancer and metastasis. *Adv Sci*. 2023;10:e2300878.
8. He K, Chen D, Zhu D, et al. Drug-loaded indocyanine green J-aggregates activate metalloimmunotherapy for sustained photothermal therapy of hepatocellular carcinoma. *J Nanobiotechnology*. 2025;23(1):317. doi:10.1186/s12951-025-03353-7
9. Li B, Luo Y, Liu G, et al. NIR-II-absorbing NDI polymer with superior penetration depth for enhanced photothermal therapy efficiency of hepatocellular carcinoma. *Int J Nanomed*. 2024;19:6577–6588. doi:10.2147/IJN.S465631
10. Wang Y, Li S, Ren X, et al. Nano-engineering nanomedicines with customized functions for tumor treatment applications. *J Nanobiotechnology*. 2023;21(1):250. doi:10.1186/s12951-023-01975-3
11. Wei W, Wang H, Ren C, et al. Ultrasmall enzyodynamic PANoptosis nano-inducers for ultrasound-amplified hepatocellular carcinoma therapy and lung metastasis inhibition. *Adv Mater*. 2024;36:e2409618.
12. Farokhi M, Mottaghitalab F, Saeb MR, Thomas S. Functionalized theranostic nanocarriers with bio-inspired polydopamine for tumor imaging and chemo-photothermal therapy. *J Control Release*. 2019;309:203–219. doi:10.1016/j.jconrel.2019.07.036
13. Overchuk M, Weersink RA, Wilson BC, Zheng G. Photodynamic and photothermal therapies: synergy opportunities for nanomedicine. *ACS Nano*. 2023;17(9):7979–8003. doi:10.1021/acsnano.3c00891
14. Tian L, Li X, Ji H, et al. Melanin-like nanoparticles: advances in surface modification and tumour photothermal therapy. *J Nanobiotechnology*. 2022;20:485.
15. Zhi D, Yang T, O'Hagan J, et al. Photothermal therapy. *J Control Release*. 2020;325:52–71. doi:10.1016/j.jconrel.2020.06.032
16. Feng T, Zhou L, Wang Z, et al. Dual-stimuli responsive nanotheranostics for mild hyperthermia enhanced inhibition of Wnt/beta-catenin signaling. *Biomaterials*. 2020;232:119709.
17. Zhang Y, Zhang L, Gao J, Wen L. Pro-death or pro-survival: contrasting paradigms on nanomaterial-induced autophagy and exploitations for cancer therapy. *Acc Chem Res*. 2019;52(11):3164–3176. doi:10.1021/acs.accounts.9b00397
18. Debnath J, Gammoh N, Ryan KM. Autophagy and autophagy-related pathways in cancer. *Nat Rev Mol Cell Biol*. 2023;24:560–575.
19. Wu PF, Chiu CC, Chen CY, Wang HM. 7-Hydroxydehydronuciferine induces human melanoma death via triggering autophagy and apoptosis. *Exp Dermatol*. 2015;24(12):930–935. doi:10.1111/exd.12805
20. Kwon J, Huang X, Lee J, et al. Biodegradable PLGA particles with confined water for safe photothermal biomodulation. *ACS Nano*. 2025;19(21):20225–20236. doi:10.1021/acsnano.5c06276
21. Chen Y, Shen J, Yuan M, et al. Dehydrocostus lactone suppresses gastric cancer progression by targeting ACLY to inhibit fatty acid synthesis and autophagic flux. *J Adv Res*. 2025;67:331–348. doi:10.1016/j.jare.2024.01.028
22. Dong T, Jiang J, Zhang H, et al. PFP@PLGA/Cu(12)Sb(4)S(13)-mediated PTT ablates hepatocellular carcinoma by inhibiting the RAS/MAPK/MT-CO1 signaling pathway. *Nano Converg*. 2021;8(1):29. doi:10.1186/s40580-021-00279-2
23. Yang Q, Li P, Ran H, et al. Polypyrrole-coated phase-change liquid perfluorocarbon nanoparticles for the visualized photothermal-chemotherapy of breast cancer. *Acta Biomater*. 2019;90:337–349. doi:10.1016/j.actbio.2019.03.056
24. Alvi SB, Appidi T, Deepak BP, et al. The "nano to micro" transition of hydrophobic curcumin crystals leading to in situ adjuvant depots for Au-liposome nanoparticle mediated enhanced photothermal therapy. *Biomater Sci*. 2019;7(9):3866–3875. doi:10.1039/C9BM00932A

25. Appidi T, SR P, Chinchulkar SA, et al. A plasmon-enhanced fluorescent gold coated novel lipo-polymeric hybrid nanosystem: synthesis, characterization and application for imaging and photothermal therapy of breast cancer. *Nanoscale*. 2022;14(25):9112–9123. doi:10.1039/D2NR01378A
26. Huang F, Wang BR, Wang YG. Role of autophagy in tumorigenesis, metastasis, targeted therapy and drug resistance of hepatocellular carcinoma. *World J Gastroenterol*. 2018;24(41):4643–4651. doi:10.3748/wjg.v24.i41.4643
27. Amaravadi RK, Kimmelman AC, Debnath J. Targeting autophagy in cancer: recent advances and future directions. *Cancer Discov*. 2019;9(9):1167–1181. doi:10.1158/2159-8290.CD-19-0292
28. Zhou Z, Yan Y, Hu K, et al. Autophagy inhibition enabled efficient photothermal therapy at a mild temperature. *Biomaterials*. 2017;141:116–124. doi:10.1016/j.biomaterials.2017.06.030
29. Wu YH, Chen RJ, Chiu HW, et al. Nanoparticles augment the therapeutic window of RT and immunotherapy for treating cancers: pivotal role of autophagy. *Theranostics*. 2023;13(1):40–58. doi:10.7150/thno.77233
30. Zou W, Hao J, Wu J, et al. Biodegradable reduce expenditure bioreactor for augmented sonodynamic therapy via regulating tumor hypoxia and inducing pro-death autophagy. *J Nanobiotechnology*. 2021;19(1):418. doi:10.1186/s12951-021-01166-y
31. Cai L, Sun T, Han F, et al. Degradable and piezoelectric hollow ZnO heterostructures for sonodynamic therapy and pro-death autophagy. *J Am Chem Soc*. 2024;146(49):34188–34198. doi:10.1021/jacs.4c14489
32. Xiao C, Sun Y, Fan J, et al. Engineering cannabidiol synergistic carbon monoxide nanocomplexes to enhance cancer therapy via excessive autophagy. *Acta Pharm Sin B*. 2023;13(11):4591–4606. doi:10.1016/j.apsb.2023.05.019
33. Zhou Z, Yan Y, Wang L, et al. Melanin-like nanoparticles decorated with an autophagy-inducing peptide for efficient targeted photothermal therapy. *Biomaterials*. 2019;203:63–72. doi:10.1016/j.biomaterials.2019.02.023
34. Qi Q, Li R, Li HY, et al. Identification of the anti-tumor activity and mechanisms of nuciferine through a network pharmacology approach. *Acta Pharmacol Sin*. 2016;37(7):963–972. doi:10.1038/aps.2016.53
35. Fang J, Islam W, Maeda H. Exploiting the dynamics of the EPR effect and strategies to improve the therapeutic effects of nanomedicines by using EPR effect enhancers. *Adv Drug Deliv Rev*. 2020;157:142–160. doi:10.1016/j.addr.2020.06.005
36. Shi Y, van der Meel R, Chen X, Lammers T. The EPR effect and beyond: strategies to improve tumor targeting and cancer nanomedicine treatment efficacy. *Theranostics*. 2020;10(17):7921–7924. doi:10.7150/thno.49577
37. Zhang X, Tang J, Li C, et al. A targeting black phosphorus nanoparticle based immune cells nano-regulator for photodynamic/photothermal and photo-immunotherapy. *Bioact Mater*. 2020;6(2):472–489. doi:10.1016/j.bioactmat.2020.08.024
38. Appidi T, Pemmaraju DB, Khan RA, et al. Light-triggered selective ROS-dependent autophagy by bioactive nanoliposomes for efficient cancer theranostics. *Nanoscale*. 2020;12(3):2028–2039. doi:10.1039/C9NR05211A
39. Du X, Di Malta C, Fang Z, et al. Nuciferine protects against high-fat diet-induced hepatic steatosis and insulin resistance via activating TFEB-mediated autophagy–lysosomal pathway. *Acta Pharm Sin B*. 2022;12(6):2869–2886. doi:10.1016/j.apsb.2021.12.012
40. Tan A, Prasad R, Lee C, Jho EH. Past, present, and future perspectives of transcription factor EB (TFEB): mechanisms of regulation and association with disease. *Cell Death Differ*. 2022;29(8):1433–1449. doi:10.1038/s41418-022-01028-6
41. Settembre C, Di Malta C, Polito VA, et al. TFEB links autophagy to lysosomal biogenesis. *Science*. 2011;332(6036):1429–1433. doi:10.1126/science.1204592
42. Kotsiliti E. NAFLD incidence is increasing. *Nat Rev Gastroenterol Hepatol*. 2023;20:344.
43. Wong VW, Ekstedt M, Wong GL, Hagstrom H. Changing epidemiology, global trends and implications for outcomes of NAFLD. *J Hepatol*. 2023;79(3):842–852. doi:10.1016/j.jhep.2023.04.036
44. Yip TC, Lee HW, Chan WK, et al. Asian perspective on NAFLD-associated HCC. *J Hepatol*. 2022;76(3):726–734. doi:10.1016/j.jhep.2021.09.024